

Photodeposited polyamorphous CuO_x hole-transport layers in organic photovoltaics

Nicholas M. Randell,^{†,‡} Renaud Miclette Lamarche,^{†,‡} Francesco Tintori,[†] Roman Chernikov,[¶] Gregory C. Welch,[†] and Simon Trudel^{*,†,‡}

[†]*Department of Chemistry, University of Calgary, Calgary, AB, Canada*

[‡]*Institute for Quantum Science and Technology, University of Calgary, Calgary, AB, Canada*

[¶]*Canadian Light Source, Saskatoon, SK, Canada*

E-mail: trudels@ucalgary.ca

Phone: +1.403.210.7078

Abstract

Hole-selective charge transport layers are an important part of modern thin-film electronics, serving to direct electron flow and prevent leakage current. Crystalline metal-oxide hole-transport layers (HTLs) such as NiO and CuO_x exhibit high performance and stability. However they are traditionally not amenable to scalable and sustainable solution-processing techniques. Conversely, amorphous metal oxides are much more readily prepared by low-temperature solution processing methods but often lack the charge transport properties of crystalline semiconductors. Herein we report the fabrication of amorphous $a\text{-CuO}_x$ thin films from commercially available starting material using a simple UV-based thin-film deposition method. Subsequent thermal annealing of the $a\text{-CuO}_x$ induces an amorphous-to-amorphous phase transition resulting in p-type semiconducting behavior. The resulting thin films were used as HTLs in organic photovoltaic devices with power conversion efficiencies comparable to those fabricated with PEDOT:PSS.

1 Introduction

Many types of modern thin-film electronic devices such as organic light-emitting diodes, organic photovoltaic devices (OPVs), and perovskite solar cells require charge-selective interlayers to optimize their function. In these devices hole-transport layers (HTLs) serve to promote the movement of holes, while blocking the back-flow of electrons. Common hole-transport layers include doped organic semiconductors such as PEDOT:PSS¹⁻³ or Spiro-OMeTAD,^{2,4} and inorganic semiconductors such as MoO_x,⁵⁻⁷ BiOCl,⁸ CuO_x,⁹⁻¹³ and NiO.^{3,14-17} This latter class of HTLs, inorganic semiconductors, are sought after for their durability and stability in high-performance devices such as perovskite solar cells. Both NiO and mixed-valence CuO_x are wide band gap p-type semiconductors, their energy levels are ideal for the transport of holes from the active layer to the transparent electrode while their high conduction band levels prevent leakage current of electrons.¹⁸⁻²⁰ Typically these materials are used in their crystalline form to optimize charge carrier mobility. Traditionally, sputter-coating has been the method of choice for growing optical quality metal-oxide thin films; however the high vacuum and voltage required for sputter coating are energy intensive and not amenable to high throughput; a solution-based deposition method would be the ideal future to enable low-cost roll-to-roll processing. Unfortunately, solution processing methods common for crystalline metal-oxide semiconductors rely on high-temperature annealing steps in the case of sol-gel fabrication, or synthesis of metastable precursors in the case of nanoparticles. An ideal metal-oxide semiconductor HTL would be solution processable using inexpensive precursors, be amenable to large-scale processing techniques such as slot-die coating or spray coating, and require minimal post-deposition processing steps. One such deposition technique is the UV light-assisted decomposition of a precursor coordination complex to produce metal-oxide films.^{21,22} In this case, a photosensitive precursor is deposited as a thin film on a substrate and irradiated with short-wave UV light. Upon excitation of the ligand-to-metal charge transfer transition the metal centre is reduced to an M(0) state while the resulting ligand-based radical decomposes into

volatile side products that are eliminated from the film. When this process is performed in air the thin metal film is rapidly converted to an amorphous metal (oxy)hydroxide material. For simplicity these layers are generally (and will be in this report) referred to as metal oxides. UV decomposition-derived metal-oxide thin films are completely amorphous, and have been shown to be effective catalysts for the oxygen evolution reaction in aqueous electrocatalysis.^{21,23,24} Recently, such amorphous thin films have been used as both the electrode and active material in solid-state electrochromic windows.^{25,26} These devices demonstrated the use of photodeposited amorphous NiO_x and WO_x , paving the way for their use in other optoelectronic devices.

In this study we will outline the fabrication of amorphous copper oxide ($a\text{-CuO}_x$) using UV-decomposition of solution-processed commercially available precursor transition metal complexes. The resulting amorphous $a\text{-CuO}_x$ (by XRD) thin films were structurally characterized using x-ray absorption spectroscopy, x-ray photoelectron spectroscopy (XPS) and atomic force microscopy (AFM); additionally, their electronic properties were studied by UV/visible spectroscopy and UV photoelectron spectroscopy (UPS). It was discovered that annealing at temperatures greater than 200 °C induced an amorphous-to-amorphous phase transition without yielding a crystalline material. Finally, the $a\text{-CuO}_x$ thin films were incorporated into OPVs as the HTL. Films of the high-temperature polyamorph of $a\text{-CuO}_x$ (those annealed above 200 °C) performed comparably to control devices fabricated with PEDOT:PSS-based HTLs.

2 Results

2.1 Photodeposition of $a\text{-CuO}_x$ thin films

To create smooth, continuous films of $a\text{-CuO}_x$ we use a precursor containing large poorly crystalline aliphatic carboxylic acid ligands with an unresolved chiral centre, copper(II) bis(2-ethylhexanoate) ($\text{Cu}(\text{2-ethex})_2$).²⁷ When deposited via spin- or slot-die coating this complex forms a continuous film less prone to cracking than those of more crystalline precursors such as $\text{Cu}(\text{II})$ acetylacetonate.²² $\text{Cu}(\text{2-ethex})_2$ is also commercially available, relatively inexpensive, and is dark blue in solution

and thin film, which makes it simpler to qualitatively assess printed or cast layers before UV treatment which renders the layer light brown to colourless (see Fig. S1). In this case the precursor was amenable to spin casting – as well as roll-to-roll compatible, industrially relevant, slot-die coating – from a range of solvents; *n*-butyl acetate was determined to provide optimum layer quality while allowing us to avoid highly toxic halogenated solvents. The UV-induced decomposition of precursor films on IR-transparent CaF_2 substrates can be followed by transmission FTIR by tracking the disappearance of signals corresponding to the 2-ethylhexanoate ligand (Fig. 1). The decay of the major peaks in Fig. 1 at 2959 and 1584 cm^{-1} fit well to first-order reaction kinetics with half-lives of 8.25 and 4.25 min, respectively. For a thin film deposited from a 15 w/w% solution onto a CaF_2 window, the decomposition process was largely completed after 32 minutes; in this work substrates were left under the lamp for 2 hours, representing 14.5 half-lives for the slowest decay process, to ensure complete conversion of the precursor complex to the corresponding $\alpha\text{-CuO}_x$.

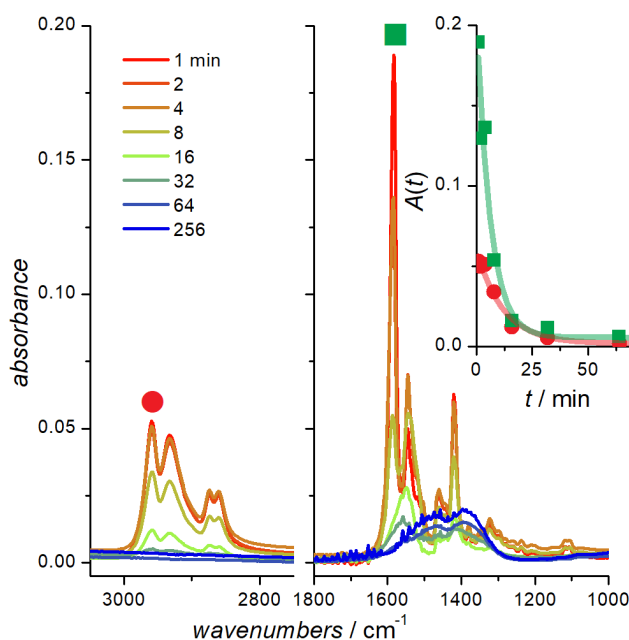


Figure 1: Evolution of the UV-driven decomposition of **Cu(2-ethex)_2** followed by FTIR spectroscopy, showing the $\nu(\text{C-H})$ (left) and $\nu(\text{COO})$ (right) bands of the 2-ethylhexanoate ligand. The decay follows a first-order reaction (inset), with lifetimes of 8.25 min and 4.25 min for the $\tilde{\nu} = 2959$ and 1584 cm^{-1} bands, respectively.

2.2 Structural Characterization of $a\text{-CuO}_x$

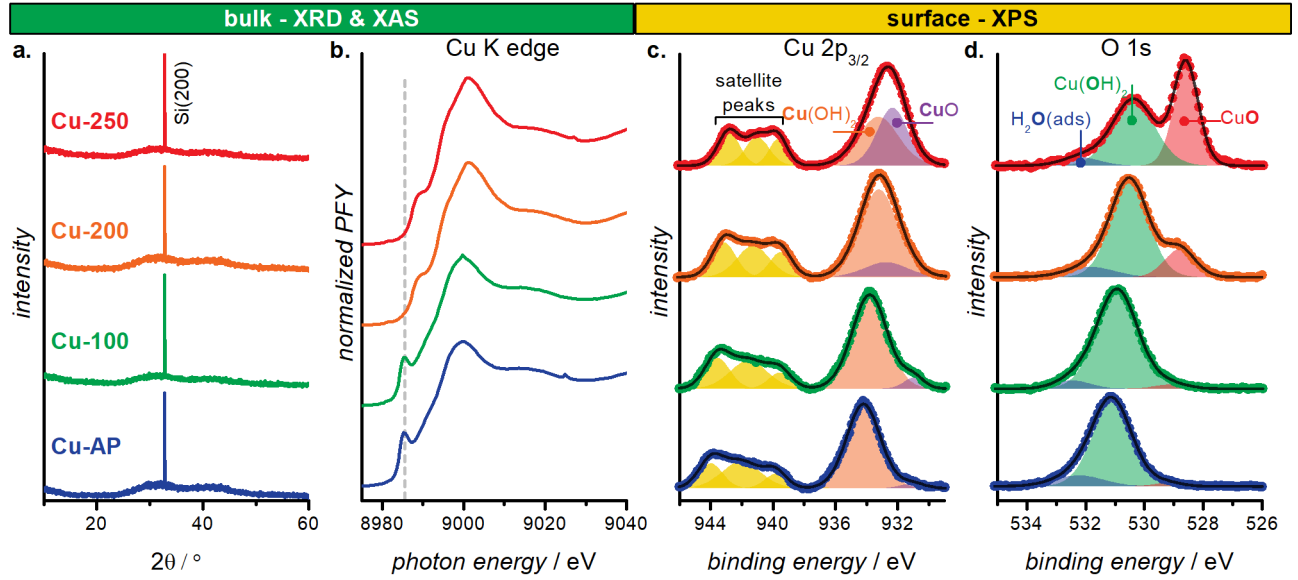


Figure 2: Bulk (a-b) and surface (c-d) physical characterization of the $a\text{-CuO}_x$ thin films. **a.** XRD measurements of $a\text{-CuO}_x$ | Si(100) thin films indicate all films are X-ray amorphous. **b.** Cu K edge XANES spectra. Cu $2p_{3/2}$ **c.** and O 1s **d.** XP spectra and associated fits show the surface of the $a\text{-CuO}_x$ films goes from Cu(OH)_2 towards CuO with increasing annealing temperature.

In order to assess the structural nature of our $a\text{-CuO}_x$ thin films, XRD patterns were collected on the as-prepared samples, and at annealing temperatures up to 250 °C. Fig. 2a demonstrates that the as-prepared films are completely amorphous with no evidence of diffraction peaks, this amorphous nature is retained up to the maximum annealing temperature of 250 °C that is tolerated by the ITO-coated substrates.²⁸

To study any short-range order that may be present in the $a\text{-CuO}_x$ structure we probed the films using X-ray absorption near-edge spectroscopy (XANES) over a series of annealing temperatures from as-prepared (AP) to 250 °C, denoted **Cu-AP**, **Cu-100**, **Cu-150**, **Cu-200**, and **Cu-250** (Fig. 2b).¹ It is immediately clear that thermal annealing has a dramatic effect on the material's structure, despite the lack of diffraction-inducing long-range order. Both the **Cu-AP** and **Cu-100** samples exhibit prominent pre-edge peaks at 8985 eV reminiscent of that seen in the

¹We note those samples were cast from 15 w/w% **Cu(2-ethex)**₂ solutions, and thus thicker than the films optimized for devices, as well as XPS and AFM measurements, which were all made with 5 w/w% **Cu(2-ethex)**₂ solutions.

crystalline Cu₂O standard (Fig. S2a), corresponding to a 1s-4p transition. At higher annealing temperatures (200 and 250 °C) the XANES spectra more strongly resemble CuO (Fig. S2b). In these cases a small pre-edge peak is observed at 8982 eV corresponding to the 1s to 3d transition (see Fig. S2b). Additionally, the rising edge 4p←1s transition is replaced by a less pronounced shoulder slightly higher in energy (8989-8990 eV) consistent with a shake-down transition (a 4p←1s transition coupled to a ligand to metal charge transfer).²⁹⁻³³ The spectra of the **Cu-200** and **Cu-250** samples are almost identical, suggesting that the structural change occurring with annealing happens at or just below 200 °C.

We characterized the *a*-CuO_x surface using XPS and atomic force microscopy on films prepared from a 5 w/w% **Cu(2-ethex)**₂ solution. The presence of satellite peaks in the Cu 2p region of the XPS spectrum is characteristic of Cu²⁺ species (Figs. 2c and S3); peak fitting revealed a mix of Cu(OH)₂ and CuO (Table S1). Fitting of the Cu 2p_{3/2} peak (Fig. 2c) indicates that the as-prepared sample's surface consists of 97% Cu(OH)₂ and 3% CuO; upon annealing the relative amount of CuO increased to a maximum of 52% CuO and 48% Cu(OH)₂ for **Cu-250** (full fitting parameters are documented in Table S1). This trend is corroborated by the O 1s peak fitting which show the hydroxide (Cu(OH)₂) peak decreasing compared to the oxide (CuO) peak (Fig. 2d). The lack of a sharp peak at lower energy in the Cu 2p_{3/2} region precludes significant amount of surface Cu⁺ or Cu⁰ species. Furthermore the ratio of the 2p_{3/2} peak and its satellite peaks remains constant with increasing annealing temperature, indicating that the ratio of Cu²⁺ to Cu⁺ or Cu⁰ is constant and that the presence of Cu⁺ remains insignificant.³⁴ The modified Auger parameter was determined for Cu. Due to the lower-resolution data of the survey scan the Cu LMM peak location is harder to determine with great precision, especially in the case of the high-temperature samples which are combination of seven peaks.³⁵ Despite this, clear signs of the shift from Cu(OH)₂ to CuO are present. The main peak shift toward higher kinetic energy, consistent with increased CuO content, and the appearance of a shoulder at 914 eV is also indicative of greater CuO presence. A small, high-energy peak in the O 1s spectra was attributed to adsorbed water³⁶ and is present at all annealing temperatures.

AFM imaging of the sample deposited onto ITO from 5 w/w% **Cu(2-ethex)₂** solutions is presented in Fig. S4. Fig. S4b,c present the surface coated with **Cu(2-ethex)₂**, before and after UV irradiation. The formation of pinholes in the film is apparent, these have a depth of around 10 nm, compared to the film surface, surrounded by protrusions that can reach up to 30 nm. This results in an increase in root-mean-squared roughness (R_{rms}) from 5.8 nm in the films before irradiation to 7.9 nm for **Cu-AP**. Increasing the annealing temperature gradually reduces the prominence of these pinholes and the roughness of the film decreases to 6.2 nm for **Cu-250**. In all cases, the *a*-CuO_x planarizes the ITO surface ($R_{\text{rms}}^{\text{ITO}} = 10.9$ nm, Fig. S4a). AFM was also used to estimate the thickness of the films by partially masking the sample from UV irradiation. It was found that the film thickness gradually decrease with annealing temperature. **Cu-AP** is around 20 nm thick, this thickness is reduced to 10 nm for **Cu-100**, and 5 nm for **Cu-200** and **Cu-250**. A similar densification of *a*-FeO_x with annealing was previously observed.²¹

2.3 Electronic Characterization

To assess the work function and valence band energy maximum of the *a*-CuO_x over the annealing series UPS was performed on *a*-CuO_x layers deposited on gold-coated Si wafers (Fig. 3). The **Cu-250** sample exhibits the lowest work function at -4.9 eV (Fig. S5), this is ideally positioned between the highest occupied molecular orbital of most typical p-type polymers used for OPV applications and the work function of ITO at 4.4-4.8 eV.³⁷ This intermediate work function should provide sufficient driving force for hole extraction from the active layer and hole injection into the ITO. The work function for *a*-CuO_x at lower annealing temperatures is at or above that of ITO.

The optical band gap and transmissivity of our *a*-CuO_x materials was measured by UV/visible spectroscopy. Using Tauc plot fitting of the UV/visible transmission spectra (Fig. S7) it was determined that the *a*-CuO_x thin films were indirect band gap semiconductors.^{38,39} The transmission UV/visible spectra reveal that the *a*-CuO_x thin films have greater than 80% transmissivity up to 340 nm for all annealing temperatures (Fig. 4). UV/visible absorbance spectra show that

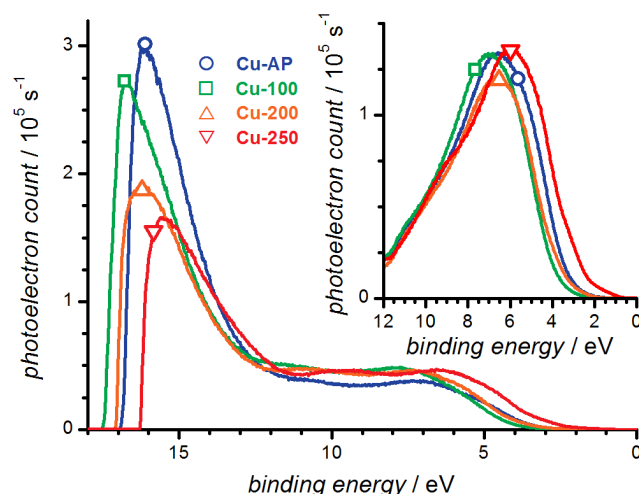


Figure 3: UPS Spectra of $a\text{-CuO}_x$ at increasing annealing temperatures, inset: valence band edge spectra.

Cu-AP samples have a slight absorbance through the visible region, this absorbance is at a minimum in the **Cu-100** sample and increases again for **Cu-200** and **Cu-250**.

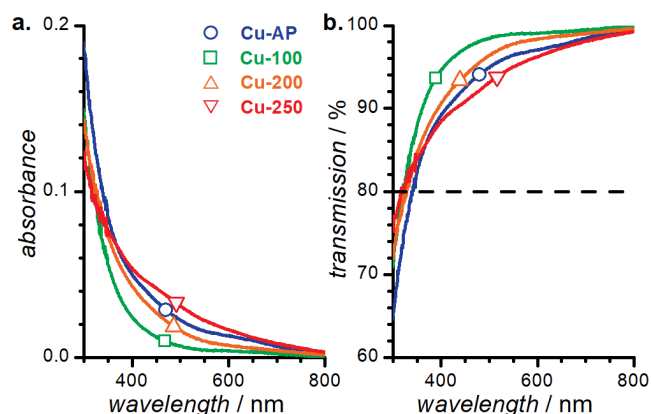


Figure 4: UV/visible a) absorbance and b) transmission spectra of $a\text{-CuO}_x$ annealed at various temperatures, showing good transparency over the visible range.

2.4 Organic photovoltaic devices

Having characterized the electronic and structural properties of the $a\text{-CuO}_x$ materials, we demonstrate their utility as HTLs in OPV applications. Devices were constructed in a normal architecture configuration of ITO/HTL/Active layer/bathocuproine/Ag. The well-studied pairing of a wide band-gap polymer (PBDB-T) and non-fullerene acceptor (ITIC-Cl) were used as the active

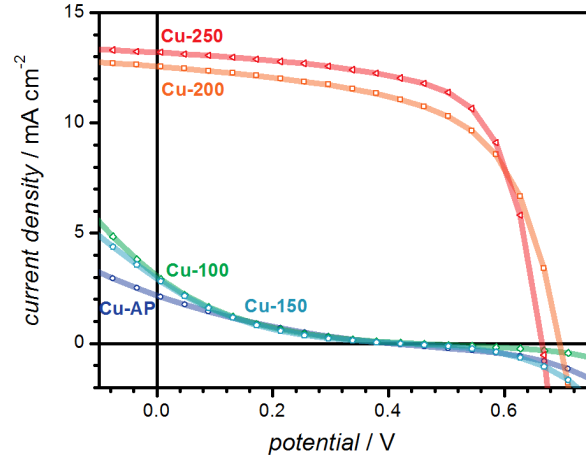


Figure 5: Current-voltage curves of OPVs with ITO/*a*-CuO_x/PBDB-T:ITIC-Cl/Cathocuprine/Ag architecture with increasing *a*-CuO_x annealing temperatures

layer components for the OPV devices.^{40–43} The thickness of *a*-CuO_x HTLs was optimized by varying spin-casting solution concentration and the optimum thickness was determined to be ~5 nm, obtained using a 5 w/w% solution of **Cu(2-ethex)**₂ in *n*-butyl acetate as measured by atomic force microscopy. OPVs were fabricated on *a*-CuO_x layers across the annealing series (Fig. 5). **Cu-AP** and **Cu-100**-based devices show an S-shaped inflection in their current-voltage (*J(V)*) curves. With increased annealing temperature charge extraction becomes balanced and the *J(V)* curve takes on a more diodic form. Device performance peaked at an annealing temperature of 250 °C (**Cu-250**), performance metrics are summarized in Table 1. Optimization of annealing time was also performed (Fig. S8), with annealing times <1 h featuring a similar S-shaped *J(V)* curve to those annealed at <200 °C. Devices with annealing times between 1 and 2 hours performed similarly, with the desired diode-shaped *J(V)* curve. When compared to a control device fabricated with a standard PEDOT:PSS hole transport layer **Cu-250**-based devices had comparable fill factors (FF) and open-circuit voltages (*V*_{OC}) with slightly reduced short-circuit current density (*J*_{SC}) (Fig. 6a). The reduced photocurrent observed in our *a*-CuO_x-based devices is demonstrated in the external-quantum-efficiency (EQE) spectra (Fig. 6b) of comparable **Cu-250** and PEDOT:PSS-based devices where a lower photocurrent is seen in the 350-500 nm region of the visible spectrum.

Table 1: Table 1: Best OPV performance of devices with normal architecture ITO/HTL/PBDB-T:ITIC-Cl/Cathocuprine/Ag

HTL	V_{OC} (V)	J_{SC} (mA cm ⁻²)	FF	PCE (%)
Cu-AP	0.40	2.18	0.18	0.16
Cu-100	0.43	3.06	0.12	0.16
Cu-200	0.70	12.5	0.60	5.3
Cu-250	0.67	13.2	0.66	5.8
PEDOT:PSS	0.68	14.1	0.67	6.4

3 Discussion

3.1 Structural evolution of *a*-CuO_x

The photoinduced decomposition of **Cu(2-ethex)**₂ to form *a*-CuO_x is driven primarily by an LMCT transition resulting in a photoreduction of the Cu metal centre and subsequent removal of the resulting radical-containing ligand fragments. When monitored by IR spectroscopy (Fig. 1) the decomposition product exhibits different decay constants for both of the most prominent stretches at 2959 and 1584 cm⁻¹. This suggests that intermediates are likely formed during the reaction. This is consistent with previous investigations into similar UV-based decomposition reactions.²² After decomposition is complete the as-prepared films are highly amorphous as assessed by x-ray diffraction in which no signal is detectable, as seen in Fig. 2a. Subsequent annealing of the films in air failed to produce any evidence of crystallization up to a maximum temperature of 250 °C. Higher annealing temperatures were not tested as the intended application of these films was as hole-transport layers deposited on ITO substrates, and ITO is known to begin to thermally degrade at temperatures higher than 250 °C.²⁸

The completely amorphous nature of our *a*-CuO_x materials required the use of synchrotron-based XANES spectroscopy in order to study any short-range ordering present in the structures. XANES spectra of *a*-CuO_x annealed at increasing temperatures revealed fascinating trends in the short-range structure of the materials. Both the **Cu-AP** and **Cu-100** samples exhibit a sharp features in the rising edge of the spectrum at 8985 eV (Fig. S2a). This is a well-known feature of Cu K-edge XANES spectra and is typically seen in Cu⁺ species with low valence coordination

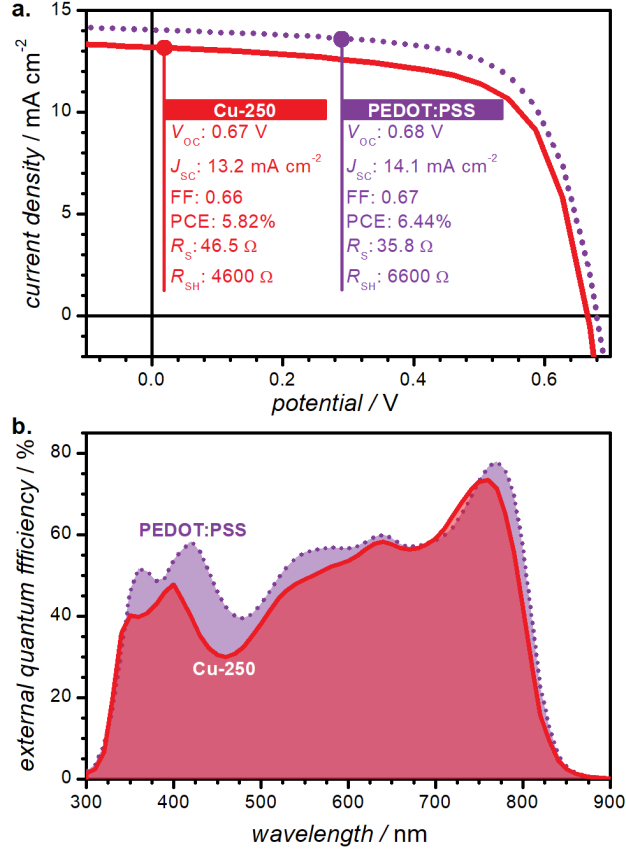
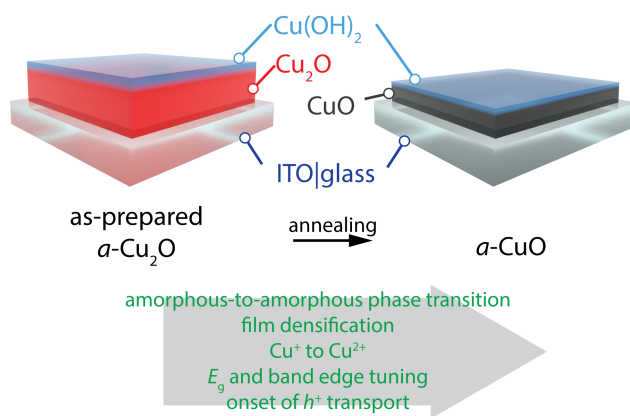


Figure 6: a) Comparing the current-voltage curve of the best-performing *a*-CuO_x-based OPV to control devices built with a PEDOT:PSS HTL shows the *a*-CuO_x devices have similar performance. The slightly lowered PCE can be attributed to a lowered J_{SC} and a decreased EQE in the 350-675 nm range (b).

modes such as 2-coordinate linear and 3-coordinate trigonal geometries, such as crystalline Cu₂O.^{29–33} In both of these spectra the pre-edge peak corresponding to a 3d←1s transition is conspicuously absent, indicating that the levels of Cu²⁺ in these species is below the detection limit. Upon annealing to 200 °C there is significant change in the Cu K edge spectrum (Figs. 2b and S2c). For both **Cu-200** and **Cu-250** the peak at 8985 eV has disappeared and been replaced by a shoulder at 8989-8990 eV ancillary to the main peak (S2b). This higher energy shoulder-peak is typical of octahedral Cu²⁺ coordination environments, and is assigned to a "shakedown" peak made up of the 4p←1s transition coupled to an LMCT transition. Additionally, a small pre-edge peak, corresponding to the 3d←1s transitions is observable in these spectra at 8982 eV. Both of these observations are consistent with a CuO-like short-range order while maintaining

long-range amorphous nature.

All of these changes in the Cu K-edge XANES spectra taken together point to the presence of an amorphous-to-amorphous phase transition in our $a\text{-CuO}_x$ thin films; in other words, we are dealing with (broadly speaking) two amorphous polymorphs of $a\text{-CuO}_x$. During this transition we move from linear low-valence coordination modes in a predominantly Cu^+ material to a primarily octahedral coordination environment with a much larger Cu^{2+} presence. Amorphous-to-amorphous phase transitions are much rarer than their counterparts in crystalline systems but have been observed in semiconductor materials such as $\alpha\text{-Si}$;⁴⁴ we recently observed similar behaviour in amorphous Ni and Fe oxyhydroxides used for electrocatalytic water splitting.^{45,46} Given that we have observed changes in electrocatalytic behavior induced by amorphous phase transitions in other materials we were immediately interested in whether these similar transitions would lead to changes in the electronic properties of our $a\text{-CuO}_x$ systems.



Scheme 1: The as-prepared films, whose bulk composition is best described as an amorphous Cu_2O , undergoes drastic modification upon annealing while retaining its amorphous nature, rendering useful amorphous CuO hole-transport layers.

In addition to X-ray absorption spectroscopy, XPS and AFM yield interesting information about the surface structure of our $a\text{-CuO}_x$ films. XPS is estimated to only probe the first 2-3 nm of the film in a $\text{CuO}/\text{Cu}(\text{OH})_2$ film. This, combined with film thickness determination using AFM, inform us on the difference between surface and bulk film (Scheme 1). **Cu-AP** and **Cu-100**

XPS reveal a surface consisting almost entirely of $\text{Cu}(\text{OH})_2$, this is at odds with XANES results, which show a sample predominantly $\text{Cu}^{\text{I}}\text{O}_2$). This is most likely a result of the surface contact with air/moisture, which allows for a more complete oxidation and formation of a hydroxide. Despite the similarity of **Cu-AP** and **Cu-100** by both XANES and XPS, AFM thickness measurements reveal that the films height halved, from around 20 nm to 10 nm. The film thickness obtained for **Cu-200** and **Cu-250** are similar (5 nm) and their XANES spectra also show little difference. However, a distinct change is observed in the XPS spectra (Fig. 2), where the relative amount of $\text{Cu}(\text{OH})_2$ decreases and the amount of CuO increases upon annealing from 200 to 250 °C. Since the thickness does not change significantly, and the XANES spectra match quite well, this can be assumed to be a surface effect, as more hydroxy-groups are lost in favor of an oxygen-terminated CuO surface during annealing. This may also explain the difference in work function between the **Cu-200** and **Cu-250** samples as well as the slight improvement in device performance.

3.2 Electronic properties and device performance of polyamorphous $a\text{-CuO}_x$

Using a combination of ultraviolet photoelectron spectroscopy and UV/visible spectroscopy we were able to assess the Fermi energy (E_F), valence band edge (E_{VB}), and optical band gap (E_g^{opt}) of the $a\text{-CuO}_x$, the results of which are summarized in an energy level diagram (Fig. 7). The E_F , as determined by secondary electron cutoff, are -4.34, -3.73, -4.12, and -4.90 eV for **Cu-AP**, **Cu-100**, **Cu-200**, and **Cu-250** respectively. The apparent trend being an increase in E_F with initial annealing to 100 °C followed by a decrease in E_F when the sample is annealed past the amorphous-to-amorphous phase transition at 200 °C. The decrease in E_F seen in **Cu-200** and **Cu-250** may be due to an increasing amount of Cu^{2+} in the structure, as suggested by the XANES results. Interestingly, the **Cu-250** sample is the only one with a low enough Fermi energy to efficiently pass holes to the ITO electrode ($E_F^{\text{ITO}} = 4.4\sim 4.5$ eV); this may help explain why OPVs fabricated from **Cu-AP** and **Cu-100** layers performed poorly. The position of the E_{VB} with respect to the E_F also changes with annealing temperature. For the **Cu-AP**, **Cu-100** and **Cu-200**

samples the E_F is further from the E_{VB} than for the **Cu-200** sample; the narrowing of the gap between E_{VB} and E_F indicates an increase in p-type character of the **Cu-250**.

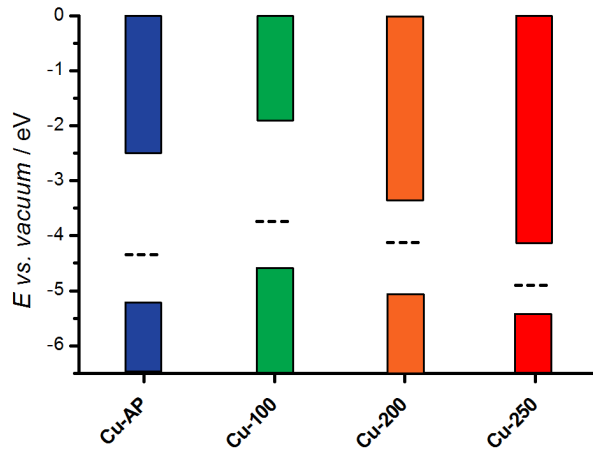


Figure 7: Frontier energy band diagram of a -CuO_x at various annealing temperatures, dashed lines indicate Fermi energy.

The evolution of the current-voltage characteristics of OPVs with a -CuO_x HTLs corroborates the evidence from our UPS data. Devices with **Cu-AP** and **Cu-100** HTLs exhibit very poor photocurrents and $J(V)$ curves with a convex shape, which is indicative of an imbalance in charge transport.^{47,48} As this is not seen with control PEDOT:PSS-based devices, it can be safely inferred that the imbalance is due to a lack of hole extraction through the low-temperature a -CuO_x polymorph HTL. This charge imbalance changes with increased annealing temperature of the a -CuO_x. When the annealing temperature is increased from 100 to 200 °C the downward inflection in the $J(V)$ curve disappears and the solar cell performance drastically improves (PCE increases from 0.16% to 5.4%) displaying a diode-like $J(V)$ curve. Upon further annealing device performance reaches a maximum between 200 and 250 °C annealing with a highest PCE to date of 5.8%.

Taken together, the change in valence band energy with increased annealing temperature along with the improvement of hole transport in the photovoltaic devices implies that the nature of the a -CuO_x is changing from that of an insulator or intrinsic semiconductor to a p-type semiconductor with increased density of holes increasing the layer's selective conductivity of positive charge. This change in electronic properties correlates very well with the change in

structure observed in the XANES spectra of the a -CuO $_x$ annealing series. As the film converts from low coordinate Cu $^+$ to a four-coordinate Cu $_2^+$ environment the doubling of positive charge must be matched by an increase in oxygen ligand content. If this charge is not fully compensated it may result in oxygen vacancies leading to a p-doped semiconductor.

This preponderance of both electronic and structural evidence leads us to the conclusion that our a -CuO $_x$ thin films are poorly conductive with low charge carrier densities as prepared. Annealing of the a -CuO $_x$ layers induces structural change and oxidation state changes resulting in p-doping of the films and an increase in hole mobility.

4 Conclusions

To summarize, we have presented the preparation of amorphous a -CuO $_x$ semiconductor thin films using mild fabrication methods from inexpensive commercially available starting materials using UV-assisted deposition techniques. As prepared, these films are poorly conducting with low charge carrier densities. Annealing at temperatures in excess of 200 °C induces an amorphous-to-amorphous phase transition which is accompanied by structural and electronic changes in the metal-oxide film that result in p-type semiconducting behavior. These p-type semiconductor thin films have been applied as the hole transport layer in thin-film organic photovoltaic devices. In these devices the a -CuO $_x$ layers function comparably to control devices using PEDOT:PSS. In conclusion, we have demonstrated that polyamorphism exhibited by amorphous metal oxide thin films can result in material phases with drastically different electronic properties, leading to dramatic improvements in thin-film electronic device performance depending on the phase used. This demonstration of the utility of amorphous transition metal oxides has the potential for a wide variety of applications in organic electronic devices.

Acknowledgement

The authors thank Alberta Innovates (Strategic Research Project grant) and the Natural Sciences and Engineering Research Council of Canada (NSERC, Discovery grant) for operating funds. This research used facilities funded by the University of Calgary, the Canadian Foundation for Innovation (John R. Evans Leaders Fund), and Research Tool and Instruments grant program of the NSERC. Funding to N.M.R was provided by the NSERC (PDF). We thank Emilio Heredia for technical assistance at the BIOXAS beamline. Part or all of the research described in this paper was performed at the Canadian Light Source (beamline proposal 31G10465), a national research facility of the University of Saskatchewan, which is supported by the Canada Foundation for Innovation (CFI), the Natural Sciences and Engineering Research Council (NSERC), the National Research Council (NRC), the Canadian Institutes of Health Research (CIHR), the Government of Saskatchewan, and the University of Saskatchewan.

Conflicts of interest

The authors declare no competing conflicts of interest.

Supporting Information Available

Experimental procedures and methods,^{49–51} and characterization data for α -CuO_x thin films.

References

- (1) Xu, H.; Yuan, F.; Zhou, D.; Liao, X.; Chen, L.; Chen, Y. Hole transport layers for organic solar cells: recent progress and prospects. *J. Mater. Chem. A* **2020**, *8*, 11478–11492.
- (2) H. Schloemer, T.; A. Christians, J.; M. Luther, J.; Sellinger, A. Doping strategies for small molecule organic hole-transport materials: impacts on perovskite solar cell performance and stability. *Chem. Sci.* **2019**, *10*, 1904–1935.

- (3) Shahnawaz,; Swayamprabha, S. S.; Ram Nagar, M.; Kumar Yadav, R. A.; Gull, S.; Kumar Dubey, D.; Jou, J.-H. Hole-transporting materials for organic light-emitting diodes: an overview. *J. Mater. Chem. C* **2019**, *7*, 7144–7158.
- (4) Ren, G.; Han, W.; Deng, Y.; Wu, W.; Li, Z.; Guo, J.; Bao, H.; Liu, C.; Guo, W. Strategies of modifying spiro-OMeTAD materials for perovskite solar cells: a review. *J. Mater. Chem. A* **2021**, *9*, 4589–4625.
- (5) Lee, K. E.; Liu, L.; Kelly, T. L. Effect of Molybdenum Oxide Electronic Structure on Organic Photovoltaic Device Performance: An X-ray Absorption Spectroscopy Study. *J. Phys. Chem. C* **2014**, *118*, 27735–27741.
- (6) Li, X.; H. Choy, W. C.; Xie, F.; Zhang, S.; Hou, J. Room-temperature solution-processed molybdenum oxide as a hole transport layer with Ag nanoparticles for highly efficient inverted organic solar cells. *J. Mater. Chem. A* **2013**, *1*, 6614–6621.
- (7) Ohisa, S.; Endo, K.; Kasuga, K.; Suzuki, M.; Chiba, T.; Pu, Y.-J.; Kido, J. Post-Treatment-Free Solution-Processed Reduced Phosphomolybdic Acid Containing Molybdenum Oxide Units for Efficient Hole-Injection Layers in Organic Light-Emitting Devices. *Inorg. Chem.* **2018**, *57*, 1950–1957.
- (8) Liu, B.; Wang, Y.; Chen, P.; Zhang, X.; Sun, H.; Tang, Y.; Liao, Q.; Huang, J.; Wang, H.; Meng, H.; Guo, X. Boosting Efficiency and Stability of Organic Solar Cells Using Ultralow-Cost BiOCl Nanoplates as Hole Transporting Layers. *ACS Appl. Mater. Interfaces* **2019**, *11*, 33505–33514.
- (9) Zuo, C.; Ding, L. Solution-Processed Cu₂O and CuO as Hole Transport Materials for Efficient Perovskite Solar Cells. *Small* **2015**, *11*, 5528–5532.
- (10) Chatterjee, S.; Pal, A. J. Introducing Cu₂O Thin Films as a Hole-Transport Layer in Efficient Planar Perovskite Solar Cell Structures. *J. Phys. Chem. C* **2016**, *120*, 1428–1437.

- (11) Hossain, M. I.; Alharbi, F. H.; Tabet, N. Copper oxide as inorganic hole transport material for lead halide perovskite based solar cells. *Sol. Energy* **2015**, *120*, 370–380.
- (12) Sun, W.; Li, Y.; Ye, S.; Rao, H.; Yan, W.; Peng, H.; Li, Y.; Liu, Z.; Wang, S.; Chen, Z.; Xiao, L.; Bian, Z.; Huang, C. High-performance inverted planar heterojunction perovskite solar cells based on a solution-processed CuO x hole transport layer. *Nanoscale* **2016**, *8*, 10806–10813.
- (13) Savva, A.; Papadas, I. T.; Tsikritzis, D.; Armatas, G. S.; Kennou, S.; Choulis, S. A. Room temperature nanoparticulate interfacial layers for perovskite solar cells via solvothermal synthesis. *J. Mater. Chem. A* **2017**, *5*, 20381–20389.
- (14) Jung, J. W.; Chueh, C.-C.; Jen, A. K.-Y. A Low-Temperature, Solution-Processable, Cu-Doped Nickel Oxide Hole-Transporting Layer via the Combustion Method for High-Performance Thin-Film Perovskite Solar Cells. *Adv. Mater.* **2015**, *27*, 7874–7880.
- (15) Kim, M.; Joo, C. W.; Kim, J. H.; Choi, W.; Lee, J.; Lee, D.; Cho, H.; Lee, H.; Park, S.; Cho, N. S.; Cho, H.; Lee, C.-W.; Jeon, D. Y.; Kwon, B.-H. Conductivity Enhancement of Nickel Oxide by Copper Cation Codoping for Hybrid Organic-Inorganic Light-Emitting Diodes. *ACS Photonics* **2018**, *5*, 3389–3398.
- (16) Kim, J. H.; Liang, P.-W.; Williams, S. T.; Cho, N.; Chueh, C.-C.; Glaz, M. S.; Ginger, D. S.; Jen, A. K.-Y. High-Performance and Environmentally Stable Planar Heterojunction Perovskite Solar Cells Based on a Solution-Processed Copper-Doped Nickel Oxide Hole-Transporting Layer. *Adv. Mater.* **2015**, *27*, 695–701.
- (17) Liu, Y.; Cai, H.; Su, J.; Ye, X.; Yang, J.; Liang, X.; Guan, J.; Zhou, X.; Yin, J.; Ni, J.; Li, J.; Zhang, J. Solution-combustion-based nickel oxide hole transport layers via fuel regulation in inverted planar perovskite solar cells. *J. Mater. Sci.: Mater. Electron.* **2020**, *31*, 15225–15232.

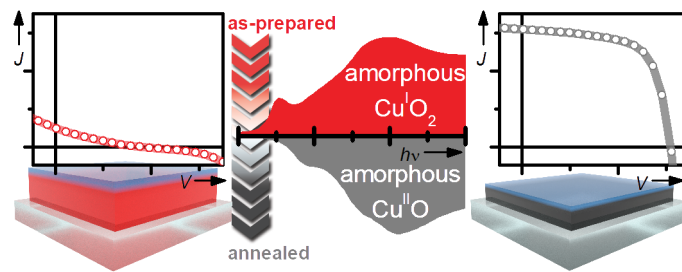
- (18) Wood, V.; Panzer, M. J.; Halpert, J. E.; Caruge, J.-M.; Bawendi, M. G.; Bulović, V. Selection of Metal Oxide Charge Transport Layers for Colloidal Quantum Dot LEDs. *ACS Nano* **2009**, *3*, 3581–3586.
- (19) Choy, W. C. H.; Zhang, D. Solution-Processed Metal Oxides as Efficient Carrier Transport Layers for Organic Photovoltaics. *Small* **2016**, *12*, 416–431.
- (20) Elseman, A. M.; Sajid, S.; Shalan, A. E.; Mohamed, S. A.; Rashad, M. M. Recent progress concerning inorganic holetransport layers for efficient perovskite solar cells. *Appl. Phys. A: Mater. Sci. Process.* **2019**, *125*, 476.
- (21) Smith, R. D. L.; Prévot, M. S.; Fagan, R. D.; Zhang, Z.; Sedach, P. A.; Siu, M. K. J.; Trudel, S.; Berlinguette, C. P. Photochemical Route for Accessing Amorphous Metal Oxide Materials for Water Oxidation Catalysis. *Science* **2013**, *340*, 60–63.
- (22) Avey, A. A.; Hill, R. H. Solid State Photochemistry of $\text{Cu}_2(\text{OH})_2(\text{O}_2\text{C}(\text{CH}_2)_4\text{CH}_3)_4$ in Thin Films: The Photochemical Formation of High-Quality Films of Copper and Copper(I) Oxide. Demonstration of a Novel Lithographic Technique for the Patterning of Copper. *J. Am. Chem. Soc.* **1996**, *118*, 237–238.
- (23) Zhang, C.; Berlinguette, C. P.; Trudel, S. Water oxidation catalysis: an amorphous quaternary Ba-Sr-Co-Fe oxide as a promising electrocatalyst for the oxygen-evolution reaction. *Chem. Commun.* **2016**, *52*, 1513–1516.
- (24) Zhang, C.; Zhang, X.; Daly, K.; Berlinguette, C. P.; Trudel, S. Water Oxidation Catalysis: Tuning the Electrocatalytic Properties of Amorphous Lanthanum Cobaltite through Calcium Doping. *ACS Catal.* **2017**, *7*, 6385–6391.
- (25) Cheng, W.; He, J.; Dettelbach, K. E.; Johnson, N. J. J.; Sherbo, R. S.; Berlinguette, C. P. Photodeposited Amorphous Oxide Films for Electrochromic Windows. *Chem* **2018**, *4*, 821–832.

- (26) Cheng, W.; Moreno-Gonzalez, M.; Hu, K.; Krzyszkowski, C.; Dvorak, D. J.; Weekes, D. M.; Tam, B.; Berlinguette, C. P. Solution-Deposited Solid-State Electrochromic Windows. *iScience* **2018**, *10*, 80–86.
- (27) Dettelbach, K. E.; He, J.; Johnson, N. J. J.; Huang, A.; Bottomley, A.; Lam, B.; Salvatore, D. A.; Berlinguette, C. P. Kinetic phases of Ag–Cu alloy films are accessible through photodeposition. *J. Mater. Chem. A* **2019**, *7*, 711–715.
- (28) Kim, Y.-N.; Shin, H.-G.; Song, J.-K.; Cho, D.-H.; Lee, H.-S.; Jung, Y.-G. Thermal Degradation Behavior of Indium Tin Oxide Thin Films Deposited by Radio Frequency Magnetron Sputtering. *J. Mater. Res.* **2005**, *20*, 1574–1579.
- (29) Baker, M. L.; Mara, M. W.; Yan, J. J.; Hodgson, K. O.; Hedman, B.; Solomon, E. I. K- and L-edge X-ray absorption spectroscopy (XAS) and resonant inelastic X-ray scattering (RIXS) determination of differential orbital covalency (DOC) of transition metal sites. *Coord. Chem. Rev.* **2017**, *345*, 182–208.
- (30) Nian, J.-N.; Chen, S.-A.; Tsai, C.-C.; Teng, H. Structural Feature and Catalytic Performance of Cu Species Distributed over TiO₂ Nanotubes. *J. Phys. Chem. B* **2006**, *110*, 25817–25824.
- (31) Gaur, A.; Shrivastava, B. D.; Joshi, S. K. Copper K-edge XANES of Cu(I) and Cu(II) oxide mixtures. *J. Phys. Conf. Ser.* **2009**, *190*, 012084.
- (32) Gaur, A.; Shrivastava, B. A Comparative Study of the Methods of Speciation Using X-ray Absorption Fine Structure. *Acta Phys. Pol. A* **2012**, *121*, 647–652.
- (33) Sharma, A.; Varshney, M.; Park, J.; Ha, T.-K.; Chae, K.-H.; Shin, H.-J. XANES, EXAFS and photocatalytic investigations on copper oxide nanoparticles and nanocomposites. *RSC Adv.* **2015**, *5*, 21762–21771.
- (34) Biesinger, M. C.; Lau, L. W.; Gerson, A. R.; Smart, R. S. Resolving surface chemical states

- in XPS analysis of first row transition metals, oxides and hydroxides: Sc, Ti, V, Cu and Zn. *Appl. Surf. Sci.* **2010**, 257, 887–898.
- (35) Biesinger, M. C. Advanced analysis of copper X-ray photoelectron spectra. *Surf. Interface Anal.* **2017**, 49, 1325–1334.
- (36) Watanabe, M.; Ando, H.; Handa, T.; Ichino, T.; Kuwaki, N. Comparative XPS Study of Silver and Copper Surfaces Exposed to Flowing Air Containing Low Concentration of Sulfur Dioxide. *Zairyo-to-Kankyo* **2007**, 56, 10–15.
- (37) Park, Y.; Choong, V.; Gao, Y.; Hsieh, B. R.; Tang, C. W. Work function of indium tin oxide transparent conductor measured by photoelectron spectroscopy. *Appl. Phys. Lett.* **1996**, 68, 2699–2701.
- (38) Makuła, P.; Pacia, M.; Macyk, W. How To Correctly Determine the Band Gap Energy of Modified Semiconductor Photocatalysts Based on UV–Vis Spectra. *J. Phys. Chem. Lett.* **2018**, 9, 6814–6817.
- (39) Tauc, J. Optical properties and electronic structure of amorphous Ge and Si. *Mater. Res. Bull.* **1968**, 3, 37 – 46.
- (40) Zhang, H.; Yao, H.; Hou, J.; Zhu, J.; Zhang, J.; Li, W.; Yu, R.; Gao, B.; Zhang, S.; Hou, J. Over 14% Efficiency in Organic Solar Cells Enabled by Chlorinated Nonfullerene Small-Molecule Acceptors. *Adv. Mater.* **2018**, 30, 1800613.
- (41) Cui, Y.; Yao, H.; Gao, B.; Qin, Y.; Zhang, S.; Yang, B.; He, C.; Xu, B.; Hou, J. Fine-Tuned Photoactive and Interconnection Layers for Achieving over 13% Efficiency in a Fullerene-Free Tandem Organic Solar Cell. *J. Am. Chem. Soc.* **2017**, 139, 7302–7309.
- (42) Zhao, W.; Qian, D.; Zhang, S.; Li, S.; Inganäs, O.; Gao, F.; Hou, J. Fullerene-Free Polymer Solar Cells with over 11% Efficiency and Excellent Thermal Stability. *Adv. Mater.* **2016**, 28, 4734–4739.

- (43) Radford, C. L.; Pettipas, R. D.; Kelly, T. L. Watching Paint Dry: Operando Solvent Vapor Annealing of Organic Solar Cells. *J. Phys. Chem. Lett.* **2020**, *11*, 6450–6455.
- (44) Morishita, T. High Density Amorphous Form and Polyamorphic Transformations of Silicon. *Phys. Rev. Lett.* **2004**, *93*, 055503.
- (45) Schoen, M. A. W.; Calderon, O.; Randell, N. M.; Jimenez-Villegas, S.; Daly, K. M.; Chernikov, R.; Trudel, S. Local structural changes in polyamorphous (Ni,Fe)Ox electrocatalysts suggest a dual-site oxygen evolution reaction mechanism. *J. Mater. Chem. A* **2021**, *9*, 13252–13262.
- (46) Schoen, M. A. W.; Randell, N. M.; Calderon, O.; Jimenez Villegas, S.; Thomson, Z.; Chernikov, R.; Trudel, S. Structural Evolution in Photodeposited Nickel (oxy)hydroxide Oxygen Evolution Electrocatalysts. *ACS Appl. Energy Mater.* **2020**, *3*, 12407–12416.
- (47) Renshaw, C. K.; Schlenker, C. W.; Thompson, M. E.; Forrest, S. R. Reciprocal carrier collection in organic photovoltaics. *Phys. Rev. B: Condens. Matter Mater. Phys.* **2011**, *84*, 045315.
- (48) Chambon, S.; Destouesse, E.; Pavageau, B.; Hirsch, L.; Wantz, G. Towards an understanding of light activation processes in titanium oxide based inverted organic solar cells. *J. Appl. Phys.* **2012**, *112*, 094503.
- (49) Nečas, D.; Klapetek, P. Gwyddion: an open-source software for SPM data analysis. *Cent. Eur. J. Phys.* **2012**, *10*, 181–188.
- (50) Ravel, B.; Newville, M. ATHENA, ARTEMIS, HEPHAESTUS: data analysis for X-ray absorption spectroscopy using IFEFFIT. *J. Synchrotron Radiat.* **2005**, *12*, 537–541.
- (51) Kraft, S.; Stümpel, J.; Becker, P.; Kuetgens, U. High resolution x-ray absorption spectroscopy with absolute energy calibration for the determination of absorption edge energies. *Rev. Sci. Instrum.* **1996**, *67*, 681–687.

TOC Graphic



Supplemental Information.

Photodeposited polyamorphous CuO_x

hole-transport layers in organic photovoltaics

Nicholas M. Randell,^{a,b} Renaud Miclette Lamarche,^{a,b} Francesco Tintori,^a
Roman Chernikov,^c Gregory C. Welch^a and Simon Trudel^{*a,b}

^a *Department of Chemistry, University of Calgary, Calgary, AB, Canada.*

^b *Institute for Quantum Science and Technology, University of Calgary, Calgary, AB, Canada.*

^c *Canadian Light Source, Saskatoon, SK, Canada.*

* E-mail: trudels@ucalgary.ca

S1 Experimental Section

S1.1 Chemicals and substrates

Cu(II) 2-ethylhexanoate (**Cu(2-ethex)**₂) was purchased from STREM Chemicals, *n*-butyl acetate was purchased from Alpha Aesar, PBDBT (70 kg/mol) and ITIC-Cl (>99% purity) were purchased from Brilliant Matters Inc, all were used without further purification. Bathocuprine was purchased from Millipore Sigma and recrystallized from toluene.

Indium-doped tin oxide ($7 \Omega/\square$) on glass substrates (ITO) were gifted from Next Energy Technologies Inc and were cleaned by sequential sonication for 10 min each in aqueous detergent solution, deionized water, and isopropanol, then stored under isopropanol until used. Immediately prior to use substrates were blown dry with N₂ and UV/ozone cleaned for 15 min. Glass substrates for UV/visible spectroscopy were cleaned using the same procedure. Si(100) substrates were prepared by cleaning in-house cut Si(100) wafers (Universiy Wafers, B-doped, 500 μm thick), using the same cleaning procedure as for the ITO substrates.

S1.2 CuO_x Thin film deposition

Cu(2-ethex)₂ was diluted to 5 wt% in *n*-butyl acetate, except in the case of the sample used for XAS and FTIR for which the casting solution concentration was 15 wt%. In all cases, the resulting precursor solution was spin coated (3000 rpm, 60 s) on clean ITO, glass, CaF₂, or Si(100) substrates. These films were then irradiated with a UV light (Atlantic UV lamp model GPH893T5VH) for 2 h, ensuring a complete decomposition of the ligands, producing a homogeneous thin film of CuO_x. The films were used as-prepared (no anneal), or annealed in air at temperatures ranging between 100 and 250 °C. Samples are labeled **Cu-AP** for the as-prepared samples and **Cu-XXX** for annealed samples, where **XXX** indicates the annealing temperature.

S1.3 OPV Fabrication and Testing

OPVs were fabricated on cleaned ITO substrates. a -CuO_x hole transport layers were fabricated as described in Section S1.2 and UV/ozone cleaned immediately before use. PEDOT:PSS HTLs were fabricated by spin casting an aqueous dispersion of PEDOT:PSS in H₂O (Clevios P-4083, filtered 0.45 μ PVDF syringe filter) at 4000 rpm for 40 s followed by annealing at 130 °C for 15 min. Active layer solutions (15 mg/ml 1:1 PBDBT:ITIC-Cl) were made by dissolving both components separately in equal volumes of *o*-dichlorobenzene. Individual solutions were stirred at 80 °C for one hour before being combined and stirred overnight at 50 °C. Active layer solutions were spin cast without filtering at 1500 rpm for 60 s. Substrates were allowed to sit for a minimum of 10 min before further coating. Bathocuprine was deposited from a 0.5 mg/ml solution in absolute ethanol (syringe filtered, 0.45 μ m PTFE) by spin casting at 4000 rpm for 60 s. Silver counter electrodes were deposited using a thermal evaporator at a maximum pressure of 1×10^{-6} mbar, at a ramped rate of 0.2 to 1 Å s⁻¹. The active device area was 0.14 cm².

Current-voltage measurements were performed in air using a Keithley 2400 Source-Measure Unit and a 100 mW cm² light source using a simulated AM1.5G filter (Newport 92251A-1000). Power intensity was calibrated using a reference Si solar cell (Newport 91150V). EQE spectra were obtained using a QEX7 Solar Cell Spectral Response/QE/IPCE Measurement System (PV Measurement, Model QEX7) with an optically focused spot size of 0.04 cm². Measurements were calibrated from 300-1100 nm using a Si photodiode.

S1.4 FTIR studies

Cu(2-ethex)₂ solutions (15 w/w% in *n*-butyl acetate) were spin cast onto optical quality CaF₂ discs (VWR Inc Part # CAAA38428-KT). Transmission spectra were collected on a Cary 630 FTIR spectrometer. Prior to deposition a blank spectrum was collected with the uncoated CaF₂ disc.

The decay of the absorbance was followed at two distinct wavenumbers $\tilde{\nu}_i$ each associated with well-resolved absorbance bands associated with the ligand, namely 2959 and 1584 cm⁻¹. The absorbance was fit to a single-order decay:

$$A(t, \tilde{\nu}_i) = A_0(\tilde{\nu}_i)e^{-k_i t} + A_{\text{offset}}(\tilde{\nu}_i) \quad (\text{S1})$$

from which a half-life $t_{1/2}$ could be determined using

$$t_{1/2} = \frac{\ln 2}{k}. \quad (\text{S2})$$

S1.5 X-ray diffraction (XRD)

XRD was performed with a Bruker D8 Advance Eco with a Cu K_α tube ($\lambda = 1.5406 \text{ \AA}$) in the $2\theta = 3 - 70^\circ$ range (step width 0.02° , 1 s averaging per step).

S1.6 Atomic force microscopy (AFM)

AFM was performed with an Agilent 5500 atomic force microscope with silicon probe (tap300DLC, Ted Pella Inc.) in tapping mode. Samples scanned for imaging were deposited onto bare ITO; samples used in layer thickness determination were deposited onto Si(100). Samples used for height determination were made by masking a portion of the precursor **Cu(2-ethex)₂** film during the UV irradiation process to prevent the formation of α -CuO_x. The samples were then rinsed in *n*-butyl acetate to selectively remove unreacted **Cu(2-ethex)₂**, yielding an area of bare Si substrate adjacent to a fully formed α -CuO_x film, allowing height determination by AFM. Data analysis was performed in Gwyddion (<http://gwyddion.net/>).⁴⁹

S1.7 X-ray absorption spectroscopy (XAS)

X-ray absorption spectra at the Cu K-edge were collected at the BioXAS beamline (main station) of the Canadian Light Source. X-ray fluorescence spectra were recorded with a 32-channel energy-discriminating Canberra Ge fluorescence detector. Spectra were acquired from 150 eV below the absorption edge to $k = 14 \text{ \AA}^{-1}$. All spectra were analyzed using the Demeter software package version 0.9.26,⁵⁰ after normalization and flattening. The energy was calibrated using the absolute energy list by Kraft,⁵¹ using a Cu foil. The following ranges were used to flatten and

normalize the XANES spectra: pre-edge range -150 to -50 eV, normalization range 200 to 700 eV.

S1.8 X-ray photoelectron spectroscopy (XPS)

X-ray photoelectron spectroscopy (XPS) was performed using a Kratos Analytical XPS spectrometer (nanoFAB Fabrication and Characterization Centre, University of Alberta) with a monochromatic Al K_{α} source ($\lambda = 1486.6$ eV) and a 2 mm^2 probing area. Samples were deposited onto gold-coated Si wafer using the same procedure as for bare Si substrates. All spectra were analyzed using CasaXPS software (<http://www.casaxps.com/>). Spectra were corrected by calibrating all peaks to the Au $4f_{7/2}$ peak signal at 83.95 eV. A Shirley-type background was used, and curve fitting was performed using a combination of Gaussian and Lorentzian [GL(30)] profiles. The analysis of the O 1s and Cu $2p_{3/2}$ region followed a methodology presented elsewhere.³⁵ Auger parameters were obtained by fitting the Cu LMM peak obtained from the survey scan.

S1.9 Ultra-violet photoelectron spectroscopy (UPS)

UPS measurements were performed using a Kratos Axis spectrometer with a source-analyser angle of 54.735600° (nanoFAB Fabrication and Characterization Centre, University of Alberta), using a He(I) UV emission line with an energy $h\nu$ of 21.21 eV.

Work functions (ϕ) were determined by linear fitting of the secondary electron cutoff (E_{se}) and using the following equation:

$$\phi = h\nu - E_{se}. \quad (\text{S3})$$

The valence band edge (E_{VB}) was determined using the minimum binding energy (E_{bind}) (determined by a linear fit of the onset of binding energy signal) and the work function according to the following equation:

$$E_{VB} = h\nu - \phi - E_{bind}. \quad (\text{S4})$$

The conduction band edge (E_{CB}) was determined by adding the optical band gap E_g (see

Section S1.10) to E_{VB} :

$$E_{CB} = E_{CB} + E_g. \quad (S5)$$

S1.10 UV-vis spectroscopy

UV-vis measurements were carried out on a UV-vis-NIR Cary 5e using thin films coated on glass substrates as per Section S1.2.

Optical band gaps were determined using the Tauc equation:

$$(\alpha h\nu)^{\frac{1}{n}} = B(h\nu - E_g) \quad (S6)$$

where $n = 1/2$ for a direct band gap transition.^{38,39}

S2 Supplemental results

S2.1 Samples

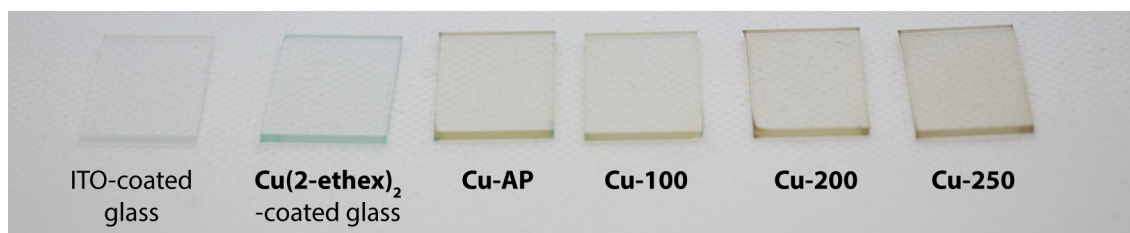


Figure S1: Photographs of (left to right): substrate, substrate coated with **Cu(2-ethex)₂**, as-prepared sample, and samples annealed at 100, 200, and 250 °C.

S2.2 XANES Spectra

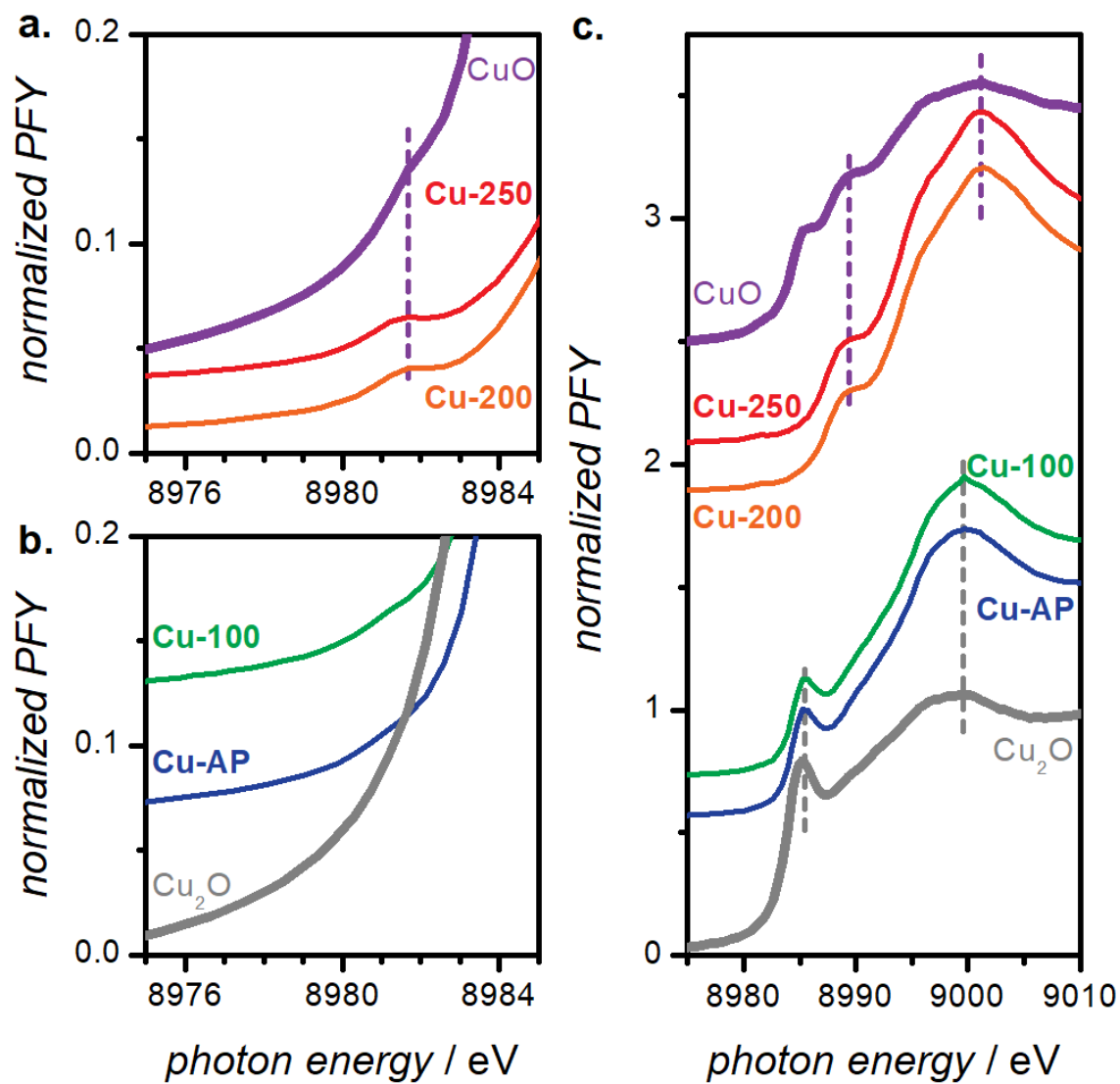


Figure S2: Cu K-edge XANES spectra with included CuO and Cu₂O standards

S2.3 Photoelectron Spectra

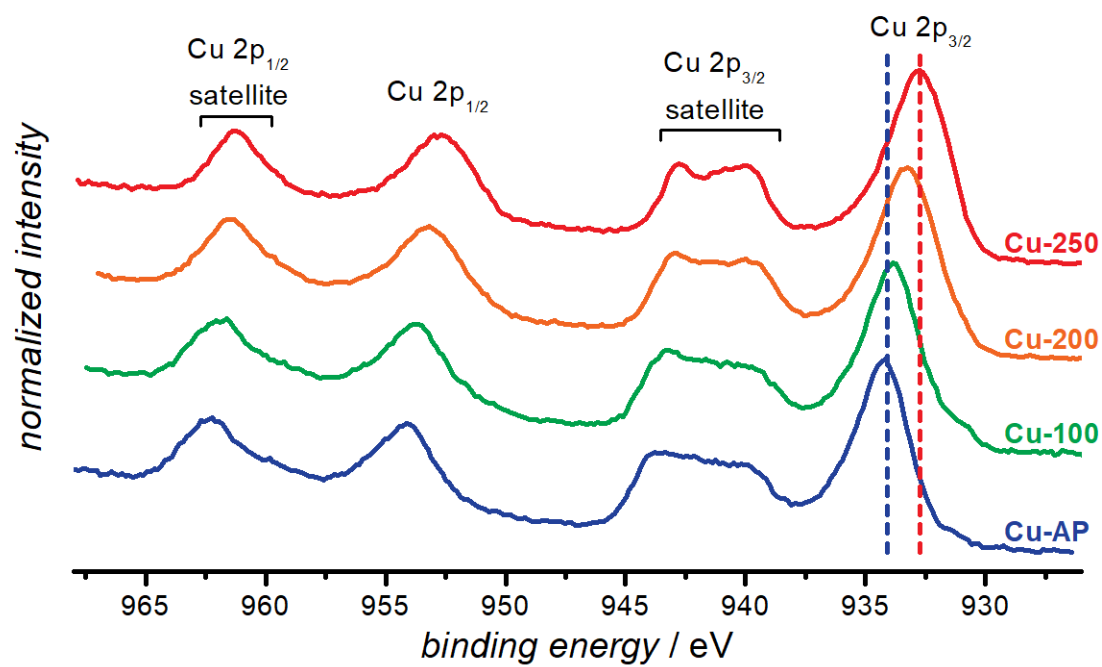


Figure S3: Cu 2p XPS spectra.

Table S1: XPS curve-fitting parameters for all samples.

Sample	Species	Line shape	Fractions ^a	Peak Position / eV	FWHM ^b / eV	Modified Auger parameter ^c / eV
Cu-AP	O 1s - H ₂ O	GL(30)	7.80	532.55	1.55	–
	O 1s - Cu(OH) ₂	GL(30)	90.54/98.2	531.12	1.61	–
	O 1s - CuO	GL(30)	1.66/1.73	529.22	0.86	–
	Cu 2p _{3/2} - Cu(OH) ₂	GL(30)	57.98/96.76	934.19	2.54	1850.50
	Cu 2p _{3/2} - CuO	GL(30)	1.94/3.24	931.13	1.43	–
	Cu 2p _{3/2} - shake ups	GL(30)	11.98,21.19,6.92	943.99,942.07,939.86	1.77,2.89,1.65	–
Cu-100	O 1s - H ₂ O	GL(30)	6.26	532.46	1.38	–
	O 1s - Cu(OH) ₂	GL(30)	90.93/97.01	530.93	1.65	–
	O 1s - CuO	GL(30)	2.80/2.99	529.09	1.18	–
	Cu 2p _{3/2} - Cu(OH) ₂	GL(30)	57.73/94.23	933.80	2.65	1850.58
	Cu 2p _{3/2} - CuO	GL(30)	3.53/5.76	931.00	1.41	–
	Cu 2p _{3/2} - shake ups	GL(30)	13.68/18.52/6.53	943.57,941.57,939.56	1.89,2.81,1.71	–
Cu-200	O 1s - H ₂ O	GL(30)	7.33	530.51	1.50	–
	O 1s - Cu(OH) ₂	GL(30)	75.52/81.49	530.51	1.50	–
	O 1s - CuO	GL(30)	17.15/18.51	528.79	1.20	–
	Cu 2p _{3/2} - Cu(OH) ₂	GL(30)	52.75/85.31	933.21	2.83	1850.33
	Cu 2p _{3/2} - CuO	GL(30)	9.08/14.69	932.76	3.27	1850.77
	Cu 2p _{3/2} - shake ups	GL(30)	13.12,16.20,8.85	943.16,941.27,393.50	1.81,2.43,1.68	–
Cu-250	O 1s - H ₂ O	GL(30)	5.99	532.16	1.56	–
	O 1s - Cu(OH) ₂	GL(30)	49.49/52.64	530.37	1.68	–
	O 1s - CuO	GL(30)	44.52/47.36	528.58	0.99	–
	Cu 2p _{3/2} - Cu(OH) ₂	GL(30)	31.72/48.25	933.35	2.89	1850.38
	Cu 2p _{3/2} - CuO	GL(30)	34.02/51.75	932.31	2.28	1851.11
	Cu 2p _{3/2} - shake ups	GL(30)	13.15,12.25,8.86	942.84,941.02,393.67	1.63,1.81,1.40	–

^a the first number includes all species, while the second excludes adventitious species and shake ups peaks, e.g. H₂O;^b FWHM = full-width half max^c ΔE between Cu 2p_{3/2} and Cu L₃M_{4,5}M_{4,5}

S2.4 Atomic Force Microscopy

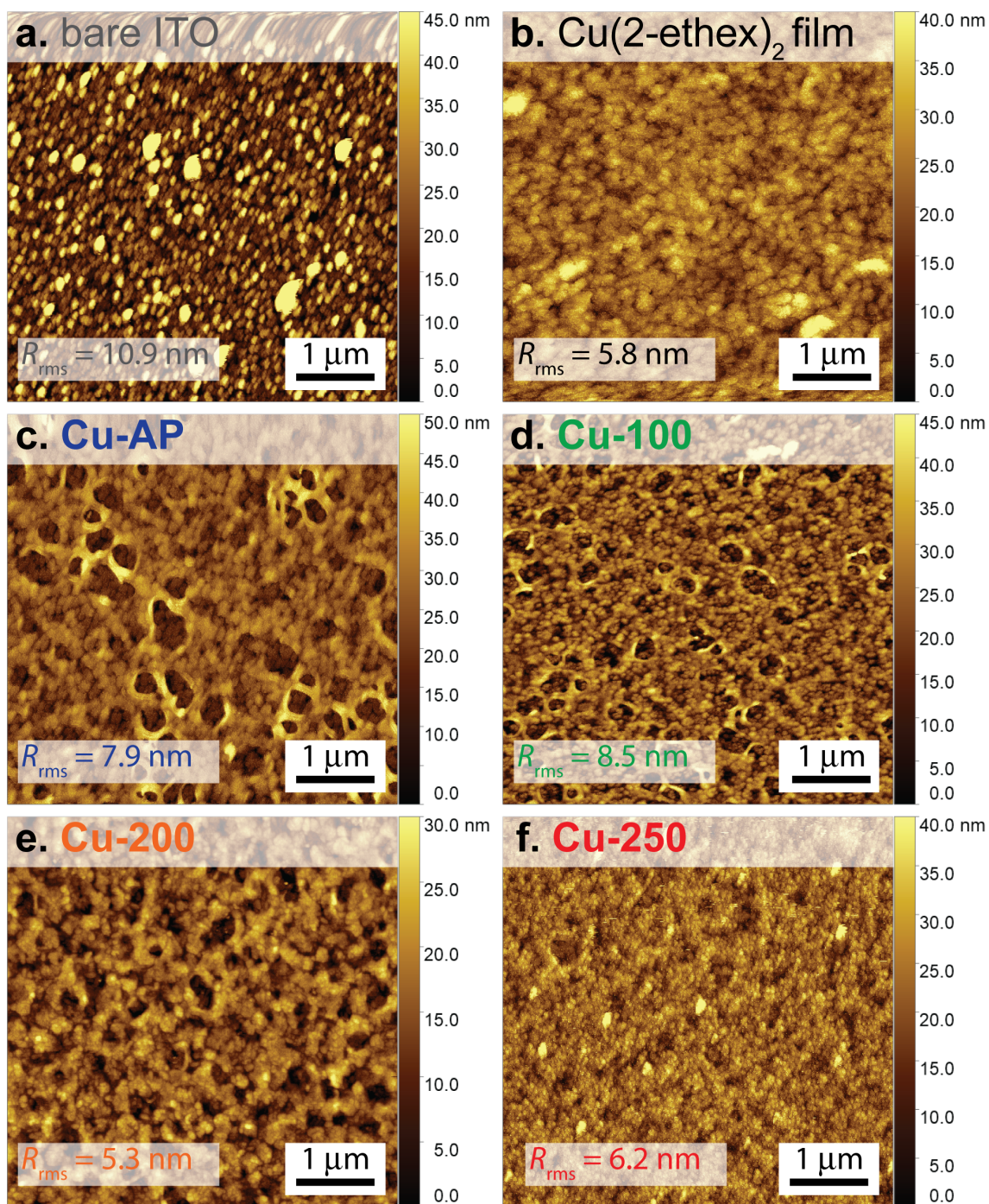


Figure S4: AFM images of $a\text{-CuO}_x$ deposited onto ITO substrate. Image are as follow: a) Bare ITO, b) Cu(2-ethex)_2 before UV irradiation, c) Cu-AP, d) Cu-100, e) Cu-200, f) Cu-250. Root-mean-squared roughness R_{rms} is indicated on each image

S2.5 Work Function Calculations from UPS

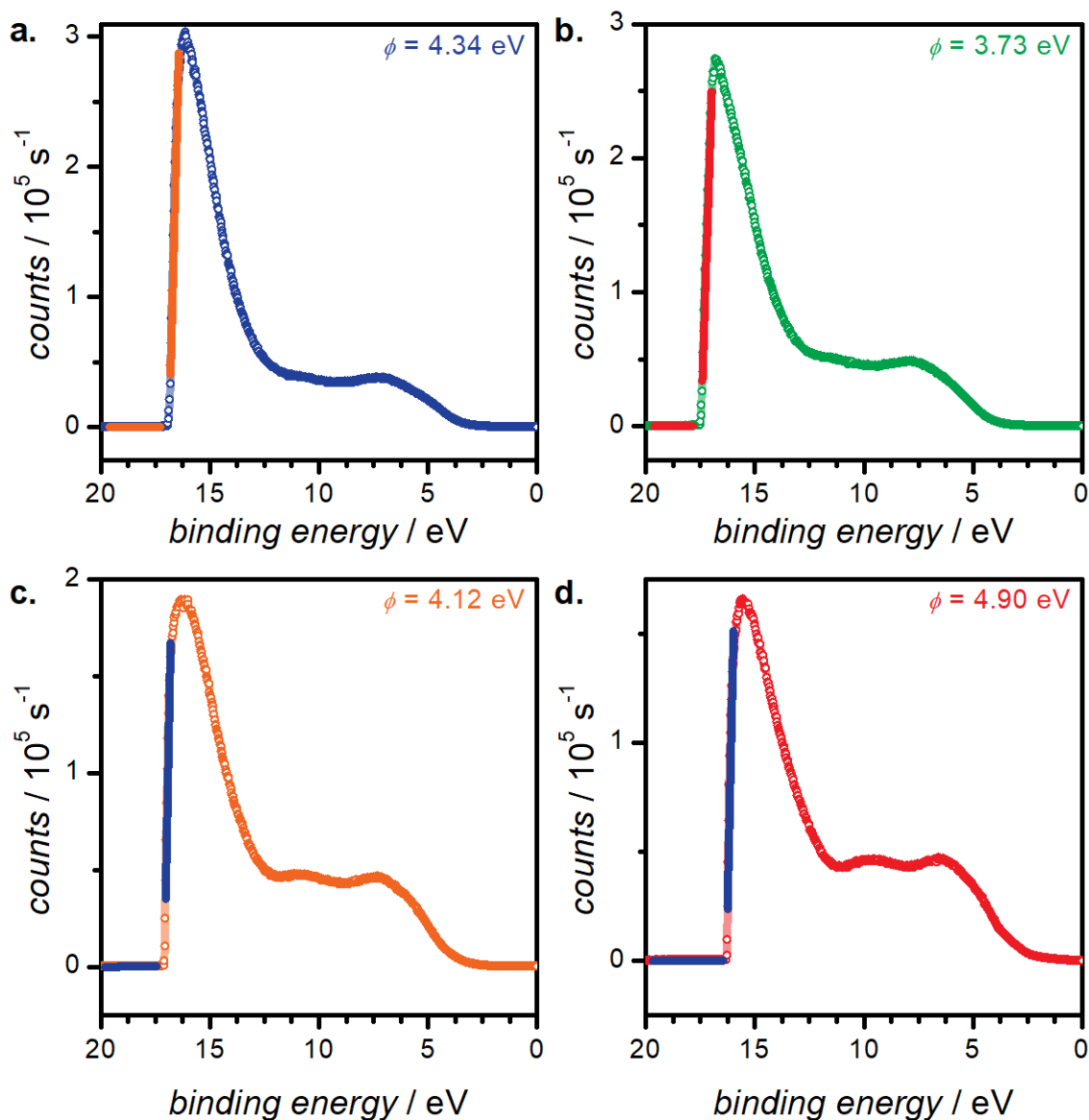


Figure S5: UP spectra used for the determination of the work function ϕ for samples **Cu-AP** (a), **Cu-100** (b), **Cu-200** (c), and **Cu-250** (d). In each spectrum, the secondary electron energy cutoff (E_{se}) is determined by extrapolating the intersection of the two linear region fits (lines).

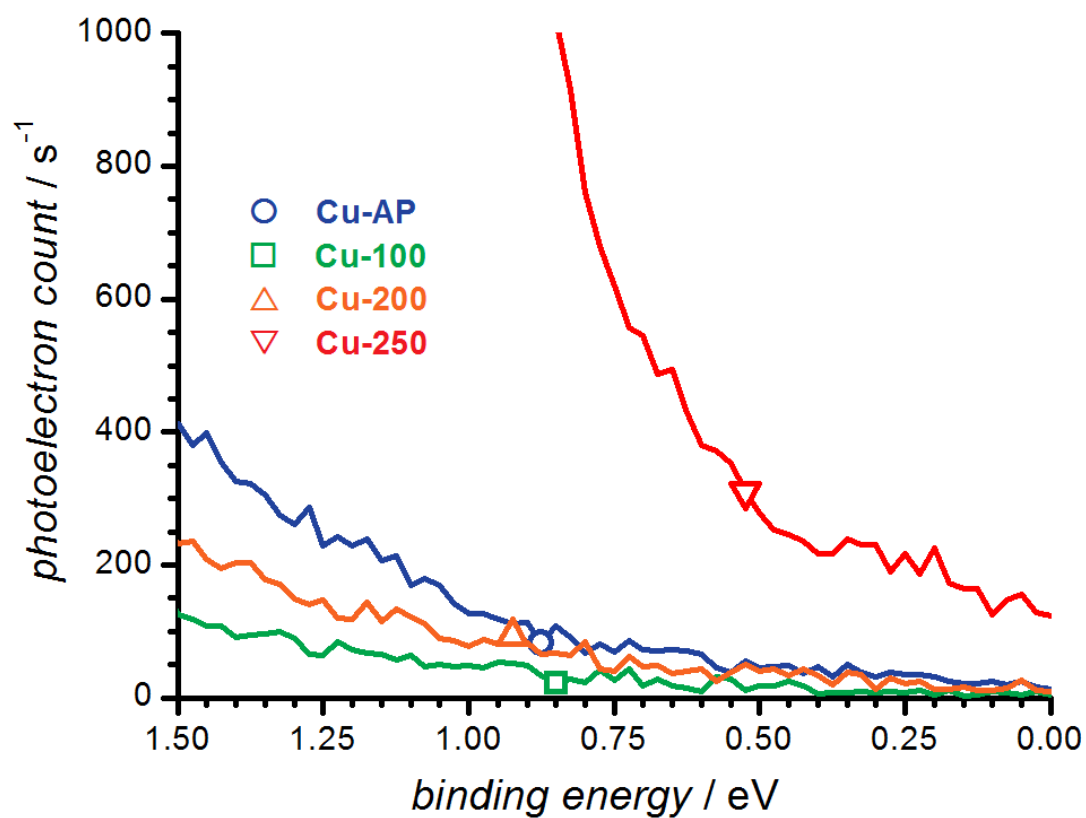


Figure S6: UP spectra used for the determination of the valence band maxima. Symbols indicate data point closest to onset of Binding Energy signal according to linear fit of the signal and background.

S2.6 Calculation of Optical Band Gaps from Tauc plots

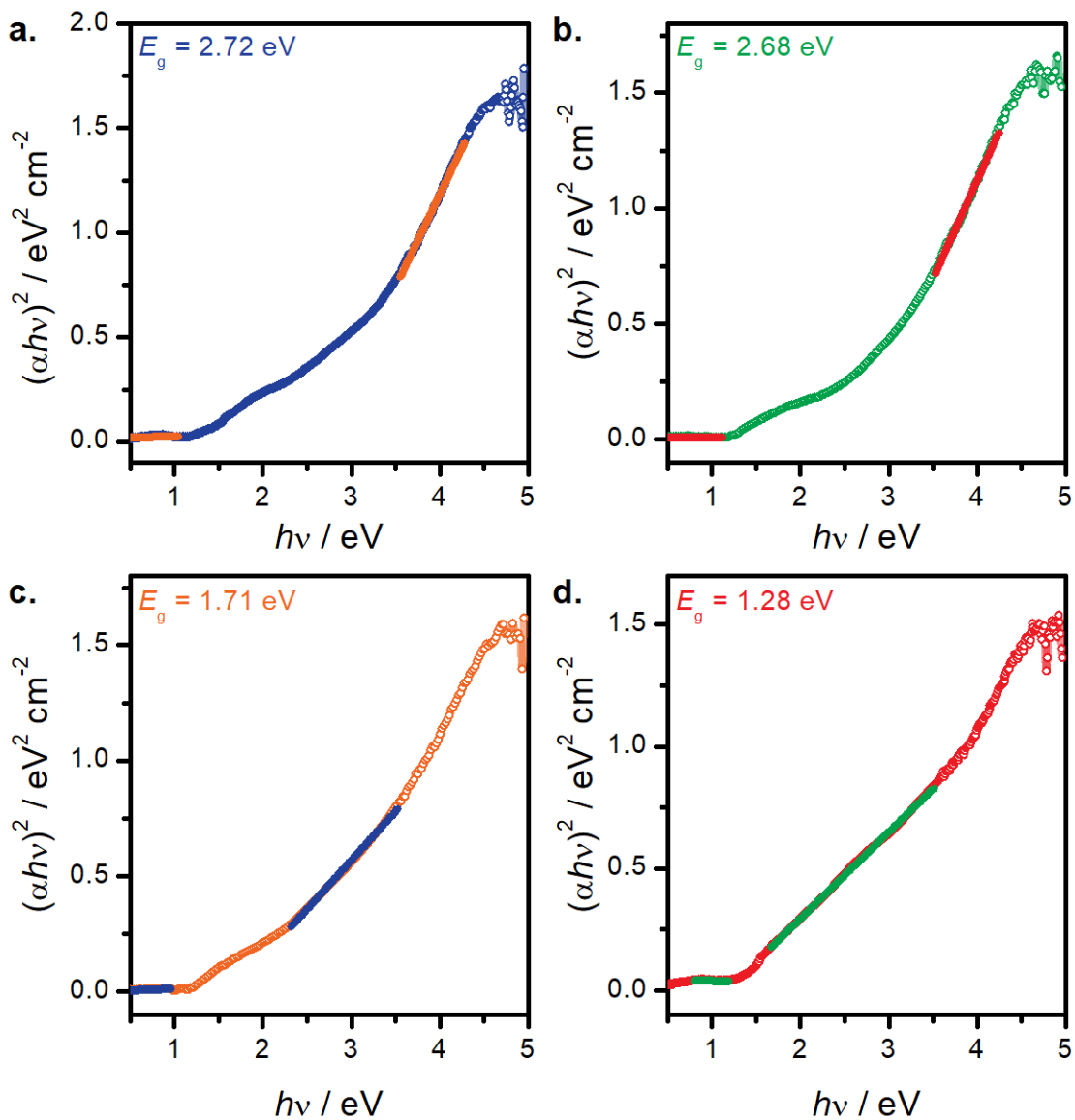


Figure S7: UV-vis spectra used for the determination of the bang gap E_g for samples **Cu-AP** (a), **Cu-100** (b), **Cu-200** (c), and **Cu-250** (d). In each spectrum, E_g is determined by extrapolating the intersection of the two linear region fits (lines).

S2.7 OPV Annealing Time Study

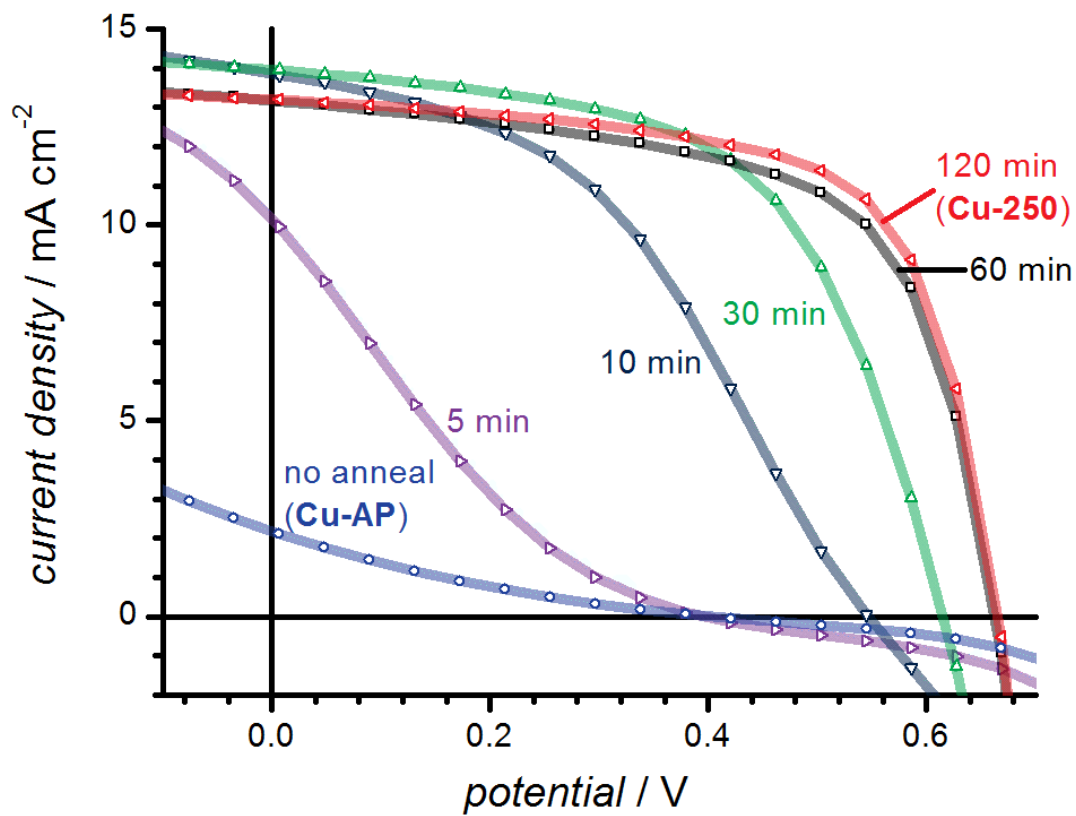


Figure S8: Current-voltage curves for OPVs with a-CuO_x layers annealed at 200-250 °C for varying times